The Astrophysical Journal Letters, 987:L6 (16pp), 2025 July 1 https://doi.org/10.3847/2041-8213/addfd0
© 2025. The Author(s). Published by the American Astronomical Society.
OPEN ACCESS

A Disintegrating Rocky World Shrouded in Dust and Gas: Mid-infrared Observations of K2-22 b Using JWST

Nick Tusay[1,2], Jason T. Wright[1,2], Thomas G. Beatty[3], Steve Desch[4], Knicole Colón[5], Tushar Mittal[6], Hugh P. Osborn[7,8], Beatriz Campos Estrada[9], James E. Owen[10], Jessica Libby-Roberts[1,2], Arvind F. Gupta[11], Brad Foley[6], Erik Meier Valdés[12], Daniel J. Stevens[13], and Ashley Herbst[4]
[1] Department of Astronomy and Astrophysics, The Pennsylvania State University, University Park, PA 16802, USA; tusay@psu.edu
[2] Center for Exoplanets and Habitable Worlds, The Pennsylvania State University, University Park, PA 16802, USA
[3] Department of Astronomy, University of Wisconsin-Madison, Madison, WI, USA
[4] School of Earth and Space Exploration, Arizona State University, P.O. Box 876004, Tempe, AZ 85287-6004, USA
[5] NASA Goddard Space Flight Center, Greenbelt, MD 20771, USA
[6] Department of Geosciences, The Pennsylvania State University, University Park, PA 16802, USA
[7] NCCR/Planet-S, Physikalisches Institut, Universität Bern, Gesellschaftsstrasse 6, 3012 Bern, Switzerland
[8] Institut für Teilchen- und Astrophysik, ETH Zürich, Wolfgang-Pauli-Strasse 27, 8093 Zürich, Switzerland
[9] Max-Planck-Institut für Astronomie, Königstuhl 17, D-69117 Heidelberg, Germany
[10] Astrophysics Group, Imperial College London, Blackett Laboratory, Prince Consort Road, London SW7 2AZ, UK
[11] U.S. National Science Foundation National Optical-Infrared Astronomy Research Laboratory, 950 N. Cherry Ave., Tucson, AZ 85719, USA
[12] Subdepartment of Astrophysics, Department of Physics, University of Oxford, Keble Road, Oxford OX1 3RH, UK
[13] Department of Physics and Astronomy, University of Minnesota Duluth, Duluth, MN 55812, USA
Received 2025 January 14; revised 2025 May 31; accepted 2025 June 3; published 2025 June 25

Abstract

The disintegrating ultrashort period rocky exoplanet K2-22 b periodically emits dusty clouds in a dynamically chaotic process resulting in a variable transit depth from 0% to 1.3%. The effluents that sublimate off the surface and condense out in space are probably representative of the formerly interior layers convectively transported to the molten surface. Transmission spectroscopy of these transiting clouds reveals spectral fingerprints of the interior composition of this rocky world. We used JWST's Mid-Infrared Instrument as a low-resolution slitless spectrograph to observe four predicted transit windows for K2-22 b. For each observation, we extracted a transmission spectrum over the spectral range of 4.4–11.8 μm. Over the spectral range of 4.4–8 μm, where the spectral precision is highest, we detect one transit at high significance and two at low significance. While the signal-to-noise ratio of the spectrum limits our ability to draw firm conclusions, we find that the data (1) disfavor featureless, iron-dominated core material, (2) are consistent with some form of magnesium silicate minerals, likely from mantle material, and (3) show a distinct and unexpected feature at $\sim$5 μm. The unexpected feature, also seen weakly in the low-significance transits, is consistent with an unknown gaseous absorber, possibly NO and/or CO_2. These findings warrant further study to improve the constraints on the composition of this disintegrating rocky world.

Unified Astronomy Thesaurus concepts: Exoplanet astronomy (486); Exoplanet atmospheres (487); Exoplanet atmospheric composition (2021); Exoplanet atmospheric variability (2020); Exoplanet structure (495); James Webb Space Telescope (2291); Transmission spectroscopy (2133)

1. Introduction

Protoplanetary disks (e.g., A. Thiabaud et al. 2015), debris disks (e.g., A. M. Hughes et al. 2018), and polluted white dwarfs (e.g., M. Jura & E. D. Young 2014; A. Vanderburg et al. 2015) provide glimpses into the constituents of planetary bodies from the beginning and end stages of a system's life cycle. Studies of such systems have also been used to assess the relationships between host-star metallicity and the material available in their planets (e.g., H. S. Wang et al. 2019; V. Adibekyan et al. 2021; M. R. Swain et al. 2024). However, these approaches, while valuable, are only indirect probes of a planet's composition. Various planetary accretion and geophysical processes can significantly impact the composition and evolution of rocky planets over their star's main-sequence phase (M. D. Ballmer & L. Noack 2021; B. J. Foley 2024).

The interior composition of terrestrial planets and its coupling with the surface atmosphere is of particular interest to the astrobiological community for assessing planetary habitability. Interpretation of planet bulk density measurements has severe compositional degeneracies, especially with regard to a planet's interior versus surface volatile reservoirs. These reservoirs are strongly influenced by geophysical processes and, in turn, impact continued planetary habitability (S. Seager et al. 2007; C. Dorn et al. 2015; C. S. Cockell et al. 2024). With only the planets in our solar system for comparison, and no clear understanding of how unique our system is, we need more observations of other systems to tease out details on interior and geophysical processes for extrasolar planets. But fully formed planets in stable orbits around main-sequence stars have a habit of keeping their rocky interiors on the inside, making the truth of their constituents difficult to access. Disintegrating exoplanets offer a unique opportunity to directly probe the interior composition of rocky exoplanets (E. H. Bodman et al. 2018). As a unique subclass of ultrashort period (USP) planets ($\lesssim$24 hr orbits), disintegrating planets are not close enough to their host star to be gravitationally disrupted but hot enough that their interior layers likely convect with a molten surface that ultimately sublimates out into space (S. Rappaport et al. 2012).

Original content from this work may be used under the terms of the Creative Commons Attribution 4.0 licence. Any further distribution of this work must maintain attribution to the author(s) and the title of the work, journal citation and DOI.

Table 1
JWST Cycle 2 GO Program 3315 and CHEOPS DDT-0020 Observation Times

Obs. No.	JWST Start and End Times (UTC)	CHEOPS Start and End Times (UTC)
1	2024 Apr 24, 16:14:02–19:13:21	2024 Apr 24, 12:24:19–21:54:33
2	2024 Apr 26, 13:57:53–16:57:11	2024 Apr 26, 09:57:08–20:02:22
3	2024 Apr 27, 08:15:54–14:19:18	2024 Apr 27, 04:34:03–14:10:16
4	2024 Apr 27, 14:21:05–20:24:29	2024 Apr 27, 14:10:16–23:46:30

K2-22 b is one of only three actively disintegrating rocky USP planets detected by the Kepler and K2 missions. K2-22 b transits a relatively bright, early M dwarf ($K = 11.91$, $T_{\rm eff} = 3830$ K) with an orbital period of 9.1457 hr (R. Sanchis-Ojeda et al. 2015). The dramatic variability in lightcurve transit depth (0%–1.3%) combined with the asymmetric transit shape suggests we are observing a transient cloud of dust sublimating off the surface of an otherwise unseen planet (S. Rappaport et al. 2012).

Having likely persisted in this state of constantly vaporizing surface material, the deeper layers of the planet may at this point be convecting to the surface or completely exposed through significant mass loss (D. A. Perez-Becker 2013; A. Curry et al. 2024). Thus, measuring the composition of these dusty effluents can probe the bulk composition of what used to be the interior of the planet (A. Curry et al. 2025). Previous studies of Kepler-1520 b (KIC 12557548b , hereafter KIC 1255 b; S. Rappaport et al. 2012) and KOI-2700 b (S. Rappaport et al. 2014), the two other previously known disintegrating USP planets, have shown through dynamical-modeling constraints that the dust in their tails might be composed of corundum (Al_2O_3 [s]) or iron-rich silicates, while other compositions such as pure iron or graphite have been ruled out (R. van Lieshout et al. 2014, 2016). Subsequent modeling efforts by J. Bromley & E. Chiang (2023) and B. Campos Estrada et al. (2024) have found iron-bearing silicates to be the most likely composition of the dust for K2-22 b and KIC 1255 b.

In this Letter, we present the results of the first mid-infrared spectroscopic measurements of a disintegrating exoplanet, K2-22 b. These measurements were made using the Mid-Infrared Instrument (MIRI) in low-resolution spectroscopy (LRS) mode on JWST. The primary objective of analyzing these observations is to match any spectral features with opacities from plausible compositions and assess if we are observing minerals and/or gases condensing from vaporization of planetary core or mantle/crust materials. In Section 2, we describe the JWST observations and simultaneous optical observations with the CHaracterising ExOPlanet Satellite (CHEOPS). In Section 3, we present the results of our analysis and the opacity models we used for comparison with the features seen in our spectra. In Section 4, we discuss our interpretation of the results, the implication they have for the composition of this target, the volatility of disintegrating exoplanet activity levels, and future work. The appendices include additional information to support our analysis, starting with MIRI data reduction using two independent pipelines, Appendices A.1 and A.2, and CHEOPS data reduction as well, Appendix A.3. Then, we have included additional discussion and plots detailing outlier removal, Appendix B; lightcurve fitting and uncertainty assessment, Appendix C; supporting evidence for spectral features, Appendix D; and optical data references, Appendix E.

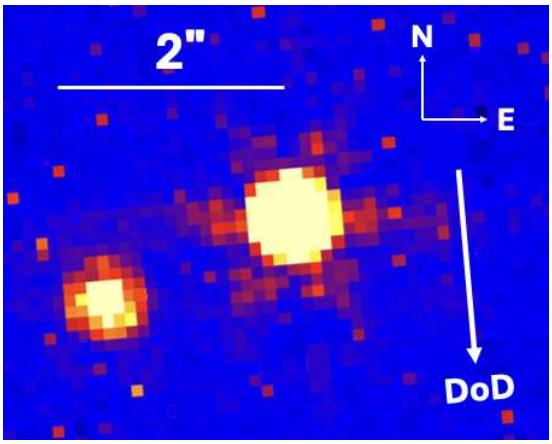


Figure 1. MIRI verification image of K2-22 and its smaller companion star, at $\sim 2''$ separation. The direction of dispersion (DOD) is included as well, showing enough separation between the binary that contamination is minimal. The DOD is $\sim 175°$ east of north.

2. Observations and Analysis

2.1. Infrared Observations with JWST

Through GO Program 3315 (PI: Wright, Science PI: Tusay), we used the MIRI LRS instrument in slitless mode on JWST to observe (a) two individual transits of K2-22 b, and (b) a full phase curve including two additional transits, using the latest available ephemeris at the time of observation scheduling from E. Schlawin et al. (2021). Table 1 provides a summary list of the observation times. The data were recorded at a cadence of 72 s. All the JWST data used in this Letter can be found in MAST at DOI: 10.17909/sxct-na33.

The roll angle of the telescope was such that the dispersion of the light was not contaminated by the companion star, spatially separated by about $2''$. Figure 1 shows the MIRI verification image of K2-22 b and its likely bound and much fainter companion ($K = 13.93$). The spatial separation is sufficiently wide to create an aperture around the target star that can collect a majority of its light without contamination by the companion. More details on the data reduction and apertures used can be found in Appendix A. The response of the slitless mode of the spectrograph extends bluer than the slit mode, yielding measurements from 4.4 to 11.8 μm.

2.2. Optical Observations with CHEOPS

CHEOPS is a 30 cm aperture space telescope optimized to observe optical (330–1100 nm) transits of exoplanets (W. Benz et al. 2021). It is located in a nadir-locked low-Earth orbit, meaning that the field rotates once every $\sim$100 minutes, with typically $\sim$40 minutes affected by Earth occultation.

We obtained three separate CHEOPS observations in a 3 day window via a Director's Discretionary Time (DDT)

Table 2
The Calculated Transit Ephemeris, Using E. Schlawin et al. (2021), and Transit Depth Measurements from the Total Combined-light MIRI Data for Each Observation of K2-22 b, Using Equations (C1) and (C2) over the Full Wavelength Range of the Detector (4.4–11.8 μm) and in Channels <8 μm

Obs. No.	Predicted Transit Center (UTC)	Transit Depth (4.4–11.8 μm) (ppm)	Depth (4.4–8 μm) (ppm)
1	2024 Apr 24, 18:01:41	22 ± 975	52 ± 253
2	2024 Apr 26, 15:45:26	972 ± 1335	727 ± 247
3	2024 Apr 27, 10:02:57	388 ± 545	446 ± 174
4	2024 Apr 27, 19:11:42	1506 ± 540	1627 ± 168

Note. The full wavelength range shows unreasonably large uncertainties, while the restricted wavelength range shows a transit with high significance (9.7σ) in the fourth observation and detections of low significance (<3σ) in observations 2 and 3.

proposal (DDT-0020, PI: Tusay) in order to constrain the optical depth of K2-22 b. These observations were simultaneous with the observations from JWST. We targeted the same individual transits and full phase curve. For the individual transits, assuming a 0.8 hr transit window, we allowed for 4.1 hr of baseline before and after each transit. Similarly, we obtained a baseline of 4.1 hr before and after the transits for the full phase curve. See Table 1 for observation times and Appendix A.3 for additional details on the CHEOPS data reduction. Analysis of the resulting lightcurve can be found in Appendix C.

3. Results

We report our best-fit transit depths in Table 2, including a detection of the transit of K2-22 b at high significance (9.7σ) during the fourth expected transit window in the combined (white) light of the MIRI instrument data when combining only channels <8 μm (i.e., where our spectra have the highest signal-to-noise ratios). We find detections of modest significance in two out of the other three transit windows, as well. The larger uncertainties in the longer wavelength data (8–11.8 μm) were deemed too unreliable for accurate measurements. We include them in our figures for completeness, but our analyses largely focused on the spectral channels from 4.4 to 8 μm. The depth uncertainties were calculated assuming uncorrelated, Gaussian noise, which we find reasonable over this wavelength range; an analysis accounting for correlated noise and non-Gaussianity (see Appendix C) suggests red noise has only a marginal effect on ($\lesssim$1.1×) the uncertainties.

Figure 2 shows the white-light time series of the second half of the phase curve, including the only significant transit event detected by JWST and the resulting transmission spectrum. Our statistical analysis of the spectrum does not include the CHEOPS data point. The CHEOPS data were primarily used to confirm no unexpectedly large optical depths during this transit, and we show them only for reference. Assuming uncorrelated white noise and examining the spectrum produced during the fourth transit window, a flat spectrum is disfavored; the reduced $\chi^2_\nu = 3.19$, increasing to $\chi^2_\nu = 3.56$ when considering only shorter wavelengths (<8 μm), and $\chi^2_\nu = 8.03$ for the most prominent features seen around 4.4–5.3 μm. These reduced χ^2_ν values are calculated between the spectrum ($R = 17$) data and the weighted mean of the spectrum (i.e., a flat spectrum).

Apparent spectral features, particularly at shorter wavelengths (<8 μm), are consistent with some combination of expected iron, magnesium, and silicate species (E. H. Bodman et al. 2018; B. Campos Estrada et al. 2024), and we find multiple species more favorably fit the data than a flat line (Figure D1 shows a Bayesian information criterion (BIC) comparison). However, the large uncertainties from the single spectrum, especially at the longer wavelengths, mean we cannot definitively distinguish between different peridotite silicates. Still, our statistical tests indicate that the iron-bearing, core-like species were more heavily disfavored than the mantle-like species. Furthermore, after analyzing a large suite of minerals, we do not find a suitable mineral with solid-state features consistent with the 4.4–5.3 μm features (and with the spectra at other wavelengths). The transit is most significantly detected at 5.1 μm, which we can match with with NO gas (see Figure 4), in contrast to a clear nondetection at 4.8 μm.

We note that MIRI has spectral foldover at the shortest wavelengths (P. Bouchet et al. 2022). While a more rigorous quantitative analysis should take this into account, the potential contamination from this effect is unlikely to entirely account for the short-wavelength features. See Appendix D for more discussion on this.

We also detect transits at low significance in two of the other three transit windows (see Figures C1 and D2). Intriguingly, in these two other transit windows, the most significant detections are in the 4.5 and 5.1 μm channels, which provides an additional line of evidence that these features in transit window 4 are real absorption features and not a statistical fluke or result of systematic uncertainties.

3.1. Solid Dust Features

We use Mie theory (G. Mie 1908) to compute the opacity of common dust species expected to be abundant in different layers of an Earth-like rocky planet. We pick Earth-like species following previous modeling results, which find them to be the most likely (J. Bromley & E. Chiang 2023; B. Campos Estrada et al. 2024). We assume the dust grain sizes to be power-law distributed between 0.01 and 5 μm, with an effective size of 1 μm and an index of 0.875. The choice of dust grain sizes is based on morphological modeling of these objects by R. Sanchis-Ojeda et al. (2015), R. van Lieshout et al. (2016), and E. Schlawin et al. (2021).

We considered Fe [s], FeO [s], and FeS [s] as minerals likely to condense after vaporization of planetary core materials. For the mantle, we considered enstatite ($MgSiO_3$ [s]), forsterite (Mg_2SiO_4 [s]), fayalite (Fe_2SiO_4 [s]), olivine ($(MgFe)_2SiO_4$ [s]), and quartz (SiO_2 [s]). We also considered corundum (Al_2O_3 [s]) as it was found to be the most likely dust species in the similar object KIC 1255 b by R. van Lieshout et al. (2016). The references for the dust optical data used are presented in Table E1. Additionally, we used the reflectance/emissivity data

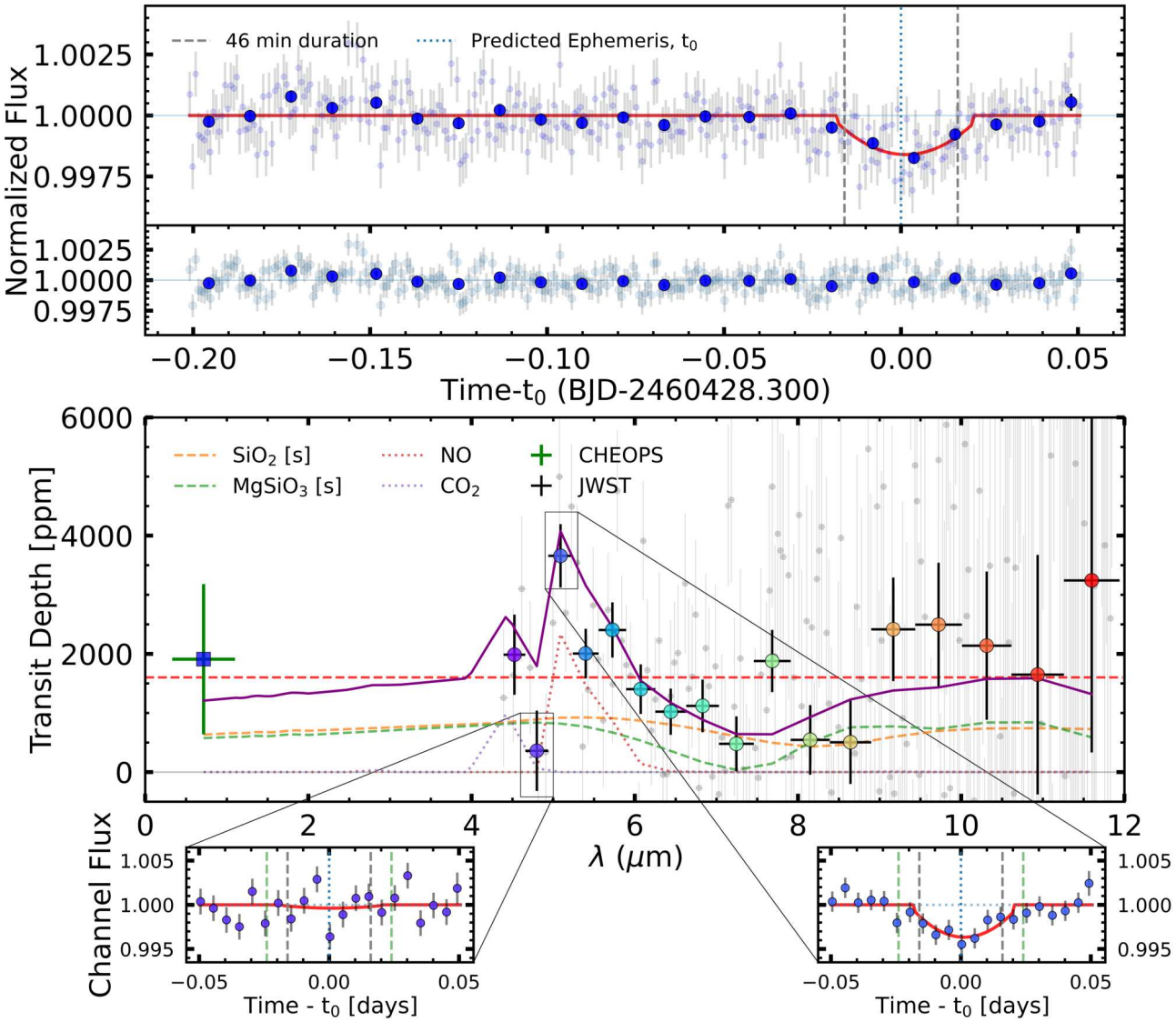


Figure 2. Results from JWST Cycle 2 GO Program 3315.

Top: lightcurve of the second half of the phase curve, collected on 2024 April 28, showing a clear transit at the predicted ephemeris. The unbinned time series data (at a cadence of 72 s) is plotted in gray in the background. The blue points are binned to a time resolution of 8 minutes. The average 46 minute duration drawn from R. Sanchis-Ojeda et al. (2015) is shown as vertical dashed gray lines for reference. Since the transit duration incorporating the cloud of material is not precisely known and potentially variable with wavelength, the baseline flux was calculated from data outside the baseline boundaries set at 1.5× the average 46 minute duration, centered at the ephemeris and shown as vertical dashed green lines. The red line is a second-order polynomial model fit to the data during transit and set to zero elsewhere. The residuals of the lightcurve model are shown in the bottom panel.

Middle: JWST MIRI spectrum showing a clear detection of a transit from 4.4 to 8 μm except at 4.8 μm. A flat spectrum is disfavored (reduced $\chi^2_\nu = 3.56$). The unbinned JWST data for each channel are plotted in gray in the background. The binned JWST spectrum in the foreground has a constant spectral resolution of $R = 17$. The horizontal red dashed line shows the overall transit depth from the MIRI lightcurve in the top panel. The dotted curves show the spectral models of plausible gas species from the DACE database (S. L. Grimm et al. 2021). The dashed curves show representative combinations of iron, magnesium, and silicate species predicted by E. H. Bodman et al. (2018) and B. Campos Estrada et al. (2024). The solid purple line shows a total opacity model representing a combination of these minerals and gases with features that plausibly correspond to features in the data. CHEOPS photometry is also shown over its 0.33–1.1 μm bandpass. The measured CHEOPS transit depth is consistent with the overall transit depth from the MIRI lightcurve.

Bottom insets: the lightcurve and transit models in two channels that illustrate an unexpected spectral feature with the most significance at ∼5 μm. The unexpected feature at 5.1 μm, consistent with nitric oxide (NO) gas is clearly detected, in contrast to a clear nondetection at 4.8 μm (see Figure 4).

from a large natural mineralogy library—JPL ECOSTRESS spectral library (S. K. Meerdink et al. 2019).

Figure 3 compares the spectrum of the fourth transit with the opacities for some of the main solid dust species we considered. The spectrum is inconsistent with featureless iron dust from a bare core (see Appendix D). The features may be consistent with some combination of solid mantle/crust mineralogy, but the significant transparency and opacity features seen at 4.4–6 μm cannot be explained by any combination of the solid dust species we considered.

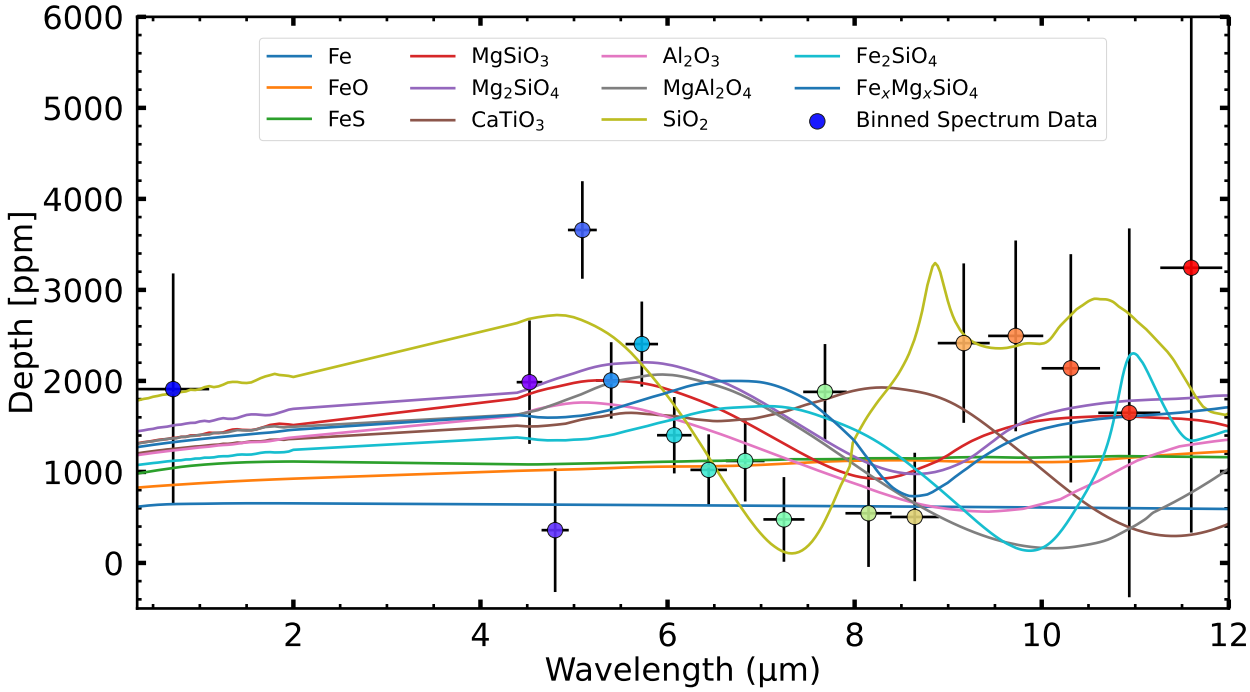


Figure 3. Opacities calculated from optical properties of solid dust species using Mie scattering theory with an effective dust grain size of 1 μm for a power-law ($p = 0.875$) distribution of dust grains. Representative models for core, mantle, and crust mineralogy are included. This spectrum disfavors purely featureless iron compounds indicative of a bare core. None of these solid dust opacities simultaneously account for all the features in the spectrum, particularly falling short of describing the feature around 5 μm.

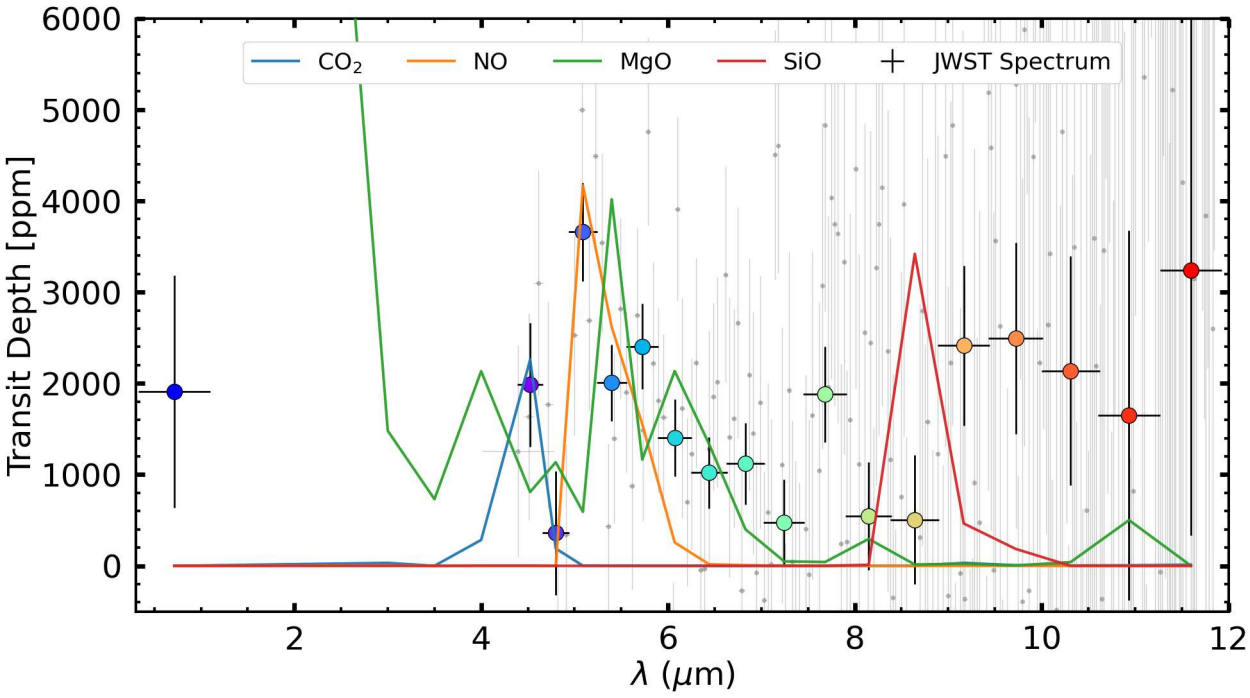


Figure 4. Gas opacities of rock and ice vapor overlaid with the MIRI data. The two most theoretically plausible species with significant mid-infrared features that are expected from typical mantle material are shown: MgO and SiO (R. A. Booth et al. 2023). These poorly fit the data, suggesting that these gases are not detected in the MIRI data. Many different ice species, binned to the same resolution as the spectral data, were considered from the DACE database. The best-fitting gas models are NO, and CO_2 to explain the short-wavelength features from 4.4 to 5.3 μm.

3.2. Gas Features

The spectrum of the fourth transit, seen in Figure 3, shows a strikingly narrow feature around 5 μm, where all solid models we considered exhibit smoothly continuous moderate opacity. This suggests the presence of a gas species. We searched the DACE database (S. L. Grimm et al. 2021) for comparable gas features and tested sets of species at high temperature (2100 K) and low pressure (10^{-8} bar) that are expected for a vaporizing

Earth-like rocky planet (e.g., L. Schaefer & B. Fegley 2009; Y. Miguel et al. 2011): CaO, TiO, AlO, MgO, and SiO. We also examined related atomic species predicted by R. A. Booth et al. (2023): Fe, Mg, and O. Figure 4 shows the resulting opacities for the two most plausible of all of these gases, MgO and SiO, with significant features in the mid-infrared. The poor fit to the data suggests these gases are not detected (as a dominant component). The optical opacity from the CHEOPS photometric measurements, despite large uncertainty, disfavors gas species with extreme optical opacity, such as Fe, Mg, O, and MgO.

Since none of the expected rock-vapor species were found to be good matches to the data, we also considered species known to be present in icy bodies in the solar system: CO, CO_2, NO, N_2, and H_2O. The resulting opacities for the two most convincing of these species, NO and CO_2, can also be seen in Figure 4. We note that the other ice species, including H_2O, are not ruled out at present. Contributions from those species are difficult to interpret with the data in hand, and a detailed analysis with more precise measurements is required to determine appropriate abundance ratios. Finally, we considered more exotic rock-vapor species: FeH, SiS, and SiN. None of the resulting opacities for these less plausible species matched the data.

4. Discussion

4.1. Composition

Assessing the habitability of rocky exoplanets requires knowledge of their interior compositions and mineralogy, which otherwise cannot be directly observed (although it can be inferred for some planets in the solar system). Although USP planets are undoubtedly inhospitable, they provide a unique case study for determining the compositions for a whole family of similar terrestrial planets and ascertaining deviations (or lack thereof) from their host-star compositions. Observations of USP planets like K2-22 b provide the opportunity to compare to observed stellar elemental abundances to constrain the interior compositions of more temperate extant rocky exoplanets.

Terrestrial rocky planets generally differentiate into metal-rich cores, rocky mantles, and chemically distinct crusts. Earth's mantle is silicate rich (mostly $MgSiO_3$ with some small Fe/Mg ratio; e.g., J. S. Kargel & J. S. Lewis 1993; H. S. C. O'Neill & H. Palme 1998). Thus, the most likely minerals to condense from a cloud of mantle vapor would be expected to be enstatite ($MgSiO_3$) and forsterite (Mg_2SiO_4). However, recent modeling by B. Campos Estrada et al. (2024) suggests a composition of magnesium–iron olivines or pyroxenes best explains the average transit shape of K2-22 b. Similarly, J. Bromley & E. Chiang (2023) argued that iron-bearing silicates are required to be able to produce an observable mass-loss rate for catastrophically evaporating exoplanets. Figure 2 demonstrates that improved long-wavelength ($\gtrsim$8 μm) spectral fidelity is critical to testing these hypotheses. However, the features seen at these longer wavelengths are at least consistent with rocky silicate, as opposed to an iron core composition.

Additionally, R. A. Booth et al. (2023) predicted opacity from likely gas species (SiO, MgO, Fe, O, and Mg) outgassing during the vaporization process, see Figure 4. The shorter MIRI wavelength features in the middle panel spectrum in Figure 2 may constitute the first direct observations of gas features from an evaporating planet. Unexpectedly, the models that best fit these measurements seem to be typically ice-derived species (NO and CO_2, see Figure 4). This is counterintuitive to what we might expect from the evaporation of a rocky mantle and demands follow-up JWST observations for verification.

One potential scenario to form these species could be photodissociation (X-ray and extreme-ultraviolet) and collisional dissociation (via energetic electrons) of molecular nitrogen and water vapor (from water ice; D. Marsh et al. 2004; M. Sinnhuber et al. 2012; M. Bulak et al. 2022). Alternatively, the NO can be produced by sublimation of H_2O and NH_3 ices followed by gas-phase chemistry through OH and NH, a mechanism that has been partially used to explain NO observations in some protostellar objects (B. M. Kulterer et al. 2024). A potential geophysical situation wherein we might get the right combination of gas and dust species (as inferred from our JWST data analysis) is the evaporation of a mantle layer with some mixture of N_2–NH_3–CO_2 ice clathrates (at the base of a deep icy ocean world; B. Journaux et al. 2020; E. Carnahan et al. 2022) and silicate minerals. An alternative possibility is that a Ceres-like body is vaporizing, with a sufficient reservoir of carbon and nitrogen in organics and ammonium-rich ices/minerals (J. Diab et al. 2023; M. C. De Sanctis et al. 2024; A. Nathues et al. 2024). This seems even more plausible given the low mass of this object inferred from previous studies (E. Schlawin et al. 2021), $\lesssim$0.03 $M_\oplus$. Another possibility is magmatic degassing of N_2, CO_2, and H_2O dissolved in an outgassing silicate magma ocean (R. Scarpa et al. 1996; E. S. Kite et al. 2016; B. Chazallon & C. Pirim 2018). The Earth's mantle is only 120 ppm C and 1–2 ppm N (W. F. McDonough & S.-s. Sun 1995; B. Johnson & C. Goldblatt 2015), suggesting that it may be difficult to get enough CO_2 and NO to explain our observations of K2-22 b, assuming it has a bulk composition similar to Earth. A potential mineralogical source for NO could be the decomposition of sinoite (Si_2N_2O), a mineral sometimes found in enstatite chondrites (K. Keil 1965), or nierite (Si_3N_4), a mineral found in enstatite and ordinary chondrites (M. R. Lee et al. 1995). However, these are rare mineral types overall and would require significant differences in mineralogical composition (e.g., high abundance of metal nitride) from what we might expect to see on Earth (e.g., in terms of planetary accretion and mantle redox state; B. Mysen 2019). Several of these scenarios imply vaporization of significant amounts of H_2O, the presence and abundance of which remains indeterminate without a more extensive analysis and more precise future measurements.

Confirming the spectral features seen for K2-22 b with additional data from JWST is critical to better assess among the various plausible geophysical scenarios discussed above by quantitatively comparing observed gas abundances with thermochemical models with gas-phase photochemistry (A. Curry et al. 2025).

4.2. Variability

K2-22 b's variable behavior has persisted well beyond the K2 mission (K. D. Colón et al. 2018; E. Schlawin et al. 2021), though recent observations indicate a long-term trend of quiescence (E. Gaidos et al. 2024). However, this is not entirely unprecedented, as the disintegrating planet KIC 1255 b has been observed with a similar reduction in activity (E. Schlawin et al. 2016), only to return to its original activity levels a few years later (E. Schlawin et al. 2018). Several

plausible interpretations for the long-term variability have been suggested: variations in stellar activity (H. Kawahara et al. 2013), changing interactions between the stellar radiation field and charged particles (D. A. Mendis & M. Horányi 2013), or substellar magma pool compositional variations (E. S. Kite et al. 2016). Long-term monitoring is required to provide observational constraints on the underlying mechanisms for this time evolution (E. Gaidos et al. 2024).

Simulations of the chaotic outflows from this class of planet have been used to show that the dynamic evolution of the transiting dust cloud model is plausible over orbital timescales (J. Bromley & E. Chiang 2023). Hydrodynamical models of dust outflow geometry suggest K2-22 b is a less massive planet than the similar object KIC 1255 b, and particles escape the surface in a manner between the extremes of purely dayside and spherical outflow (B. Campos Estrada et al. 2024). There is likely a complex interplay between the optical depth of the resulting cloud and the particles that can further condense out and add to it (J. Bromley & E. Chiang 2023). Clouds of significantly differing optical depth may exhibit variations in abundance measurements of certain compositional elements. Inhomogeneities in the material being sublimated over time could impact the dominance of iron abundance in the cloud, interacting with the stellar magnetic field, and affecting cloud formation and dissipation rates.

Optical photometry is useful to directly sample the activity level of this object, and tease out the different timescales involved. However, additional spectral measurements with JWST are crucial for linking the activity cycles with compositional differences. Reassessing the statistical distribution of K2-22 b transits at the current reduced activity levels seen in these results and E. Gaidos et al. (2024), ∼28 additional observations of individual transits with out-of-transit baseline (∼100 hr total) would offer >95% confidence in obtaining the original 0.5%–1% cumulative transit depth sought after with our original JWST program. While it may be more economical to reobserve K2-22 b with JWST only if and when it resumes higher activity levels, getting robust measurements during this quiescent phase could serve as an important point of comparison since the similarities and differences in the measured compositions between the quiescent and active phases could inform us on the physics and chemistry behind the dominant source of variability.

4.3. Looking Forward

The results of these observations have some interesting implications for the disintegrating planet model of K2-22 b. The variability and spectral features remain consistent with the ephemeral nature of a transiting cloud of dust forming dynamically from the evaporating surface material of a closely orbiting body. However, if the short-wavelength features are indeed opacity from "ice-derived" vapor species (in concert with mantle silicate components), then a terrestrial planet progenitor that formed within the snow line would be challenging to explain with traditional planet formation theories. Regardless of its composition, the close-in orbit seems plausibly explained by some migration pathway (e.g., stellar tides; S. C. Wu et al. 2024). This object must be reobserved to confirm the presence of these gas features, precisely measure the gas abundances, and determine an appropriate planetary migration and progenitor model. Additionally, getting detailed spectra during multiple phases of activity rates will constrain the impact of compositional heterogeneity on the observable variability. If these features can be confirmed in mid-infrared, then there are likely near-infrared spectral features as well that may warrant additional observations with NIRSpec. Given the overlap in wavelength range between NIRSpec and MIRI around 5 μm, this may be an effective independent strategy to verify and identify additional gas features since molecules like water and CO_2 have strong near-infrared features (L. S. Rothman et al. 2009). NIRSpec observations may be particularly important for precise measurements given the additional uncertainty in the short-wavelength range of MIRI due to possible contamination from spectral foldover, as noted in Appendix D.

The success of this experiment, despite the low precision of the measurements due to unexpectedly low activity rates, strongly validates this technique to explore the chemical composition of exoplanetary interiors and demonstrates the promise of using JWST to further explore K2-22 b and other similar targets, such as KIC 1255 b (S. Rappaport et al. 2012) and the newly discovered BD+05 4868 Ab (M. Hon et al. 2025).[14] We have categorized all of these systems together as disintegrating exoplanets, but there are several observables that make K2-22 b unique. K2-22 is the smallest/coolest host star, all of the others being mid K-type stars, leading to a low β parameter (R. Sanchis-Ojeda et al. 2015; possibly of similar value to BD+05 4868 Ab; M. Hon et al. 2025) that influences the dynamics and evolution of the outflowing material. At ∼9 hr, K2-22 b has the shortest period, allowing more observational opportunities than the other targets in a given time frame. The transit of K2-22 b is more symmetric and shorter in duration than others, showing significant forward scattering in the K2 lightcurve without the gradually decreasing posttransit depression from an extended trailing tail. The newly discovered BD+05 4868 A is significantly brighter than the other stars hosting these planets and will soon be targeted for observations, but K2-22 b offers a unique point of comparison considering the similarities and differences between the two objects. Perhaps it is an outlier or perhaps we will find similar spectral features in all of these targets. By reobserving K2-22 b and applying this technique to the other disintegrating planets, we can begin to understand how unique each system is, discover commonalities between them, and ultimately try to derive planetary interior parameters that we can trace back to the host star, which we can then apply to other systems.

Acknowledgments

This work is based on observations made with the NASA/ESA/CSA James Webb Space Telescope. The data were obtained from MAST at STScI, which is operated by the Association of Universities for Research in Astronomy, Inc., under NASA contract NAS 5-03127 for JWST. These observations are associated with GO Program 3315.

Support for GO Program 3315 was provided by NASA through a grant from the Space Telescope Science Institute, which is operated by the Association of Universities for Research in Astronomy, Inc., under NASA contract NAS 5-03127.

This material is based upon work supported by the National Science Foundation Graduate Research Fellowship Program under grant No. DGE1255832.

The work of HPO has been carried out within the framework of the NCCR PlanetS supported by the Swiss

[14] The fourth target in this category, KOI-2700 b, is significantly fainter and likely not ideal for follow-up with JWST.

National Science Foundation under grants 51NF40_182901 and 51NF40_205606.

The Center for Exoplanets and Habitable Worlds and the Penn State Extraterrestrial Intelligence Center are supported by Penn State and its Eberly College of Science.

CHEOPS is an ESA mission in partnership with Switzerland with important contributions to the payload and the ground segment from Austria, Belgium, France, Germany, Hungary, Italy, Portugal, Spain, Sweden, and the United Kingdom. The CHEOPS Consortium would like to gratefully acknowledge the support received by all the agencies, offices, universities, and industries involved. Their flexibility and willingness to explore new approaches were essential to the success of this mission. CHEOPS data analyzed in this Letter will be made available in the CHEOPS mission archive (https://cheops.unige.ch/archive_browser/).

Facilities: JWST (MIRI LRS), CHEOPS.

Software: Astropy (Astropy Collaboration et al. 2013, 2018, 2022), `Eureka!` (T. J. Bell et al. 2022), `Pegasus`.

Appendix A
Data Reduction

A.1. `Eureka!`

We reduced the Stage 0 uncal JWST data products from MAST using the `Eureka!`[15] pipeline with the standard configuration files for the MIRI instrument (T. J. Bell et al. 2022). We tested a range of apertures to account for background contamination from the companion star. Using the apertures that produced the minimum noise profiles, we ran Stage 1 to Stage 4 to obtain time series flux measurements over each observed exposure in 300 spectral channels from 4.4 to 11.8 μm. The same data reduction process was used for all four observations, with the only difference being the optimal apertures selected for each observation. We used vertical axis rows 150–393 along the dispersion axis, and horizontal axis columns 10–67. For transits 1 and 2, we selected 15 pixels for the half-width aperture around K2-22 and 25 pixels as the start of the background aperture to effectively mask out the companion. For transits 3 and 4, we used half-width apertures of 6 and 19 for the target and background, respectively.

A.2. `Pegasus`

As an independent check on the `Eureka!` data reduction described in Appendix A.1, we also reduced the observations using the `Pegasus` pipeline,[16] which has been used for NIRCam (T. G. Beatty et al. 2024; E. Schlawin et al. 2024a; L. Welbanks et al. 2024) and NIRSpec (E. Schlawin et al. 2024b) transit and eclipse observations. Our reduction began with background subtraction on the RATEINTS files provided by version 1.13.3 of the `jwst` pipeline using CRDS version 11.17.14. We first performed a general background subtraction step for each RATEINTS file by fitting a 2D, second-order spline to each integration using the entire 72×416 RATEINTS images. For the background fitting, we masked columns 0–12 and 67–723 to remove the nonimaged sections of the subarray. To prevent self-subtraction, we also masked out starlight from K2-22 by masking pixels in columns 29–45 and above row 50, and from the companion star by masking the pixels in columns 15–25 and above row 150. We then performed a single round of 3σ clipping on the unmasked portions of the image. We then fit a spline to the unmasked, unclipped pixel values with a median box size of 5 pixels. We extrapolated the combined background spline for the whole image over the masked portions near K2-22 and the companion star and subtracted it from the original image values. We then removed the alternating row and column horizontal and vertical banding in the background-subtracted images by calculating the biweight mean of each row or column, and then subtracting this mean from each row or column. In both cases, we used the same starlight mask as for the spline fitting to avoid self-subtraction.

We then extracted broadband and spectroscopic lightcurves from our background-subtracted images. To do so, we fit the

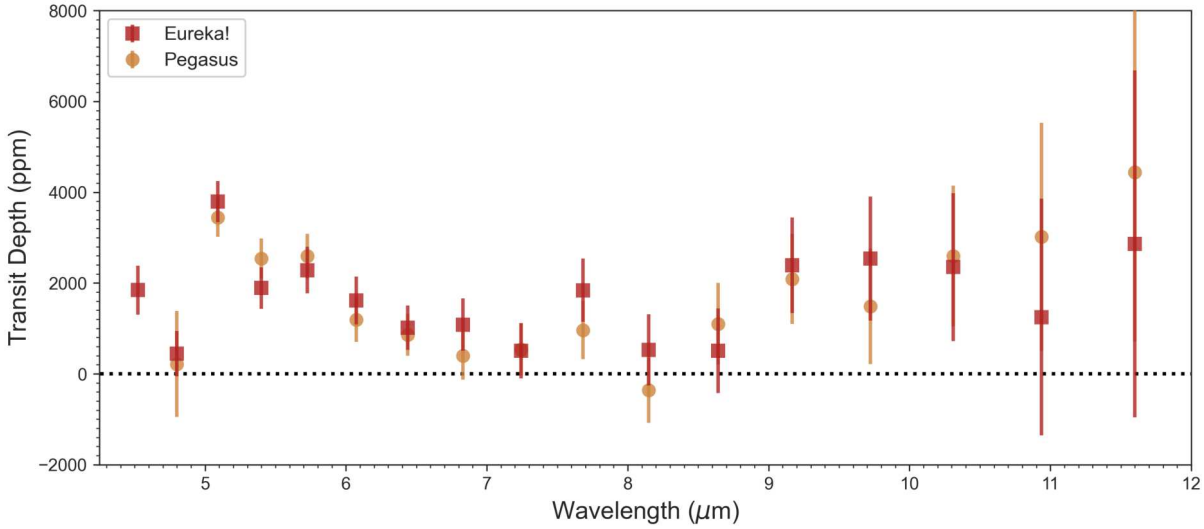


Figure A1. Two independent reductions of the MIRI LRS data for transit 4 agree within their uncertainties. Shown are our fiducial `Eureka!` results (Appendix A.1) and the results from a reduction using the `Pegasus` pipeline (Appendix A.2), plotted with their associated 1σ uncertainties at a constant spectral resolution of $R = 17$. Both reductions agree on the overall shape of the transmission spectrum and are consistent with each other to within 1σ.

[15] https://github.com/kevin218/Eureka!

[16] https://github.com/TGBeatty/PegasusProject

spectral trace using a fourth-order polynomial and then used optimal extraction to measure the 1D spectrum in each image. We performed three rounds of iterative profile estimation for the optimal extraction routine, after which we judged the profile fit to have converged. Using the resultant 1D spectra, we extracted a broadband lightcurve from 4.65 to 11.95 μm. For the spectroscopic lightcurves, we subdivided this wavelength region into 17 spectral channels spaced at a constant spectral resolution of $R = 17$. For both the broadband and spectroscopic lightcurves, we linearly interpolated over each spectral column to account for partial-pixel effects in the wavelength solutions.

Figure A1 shows that independent reduction pipelines produce good agreement of the observed transit spectrum.

A.3. CHEOPS Data Reduction

To extract precise photometry and remove systematics (e.g., due to field rotation) we used point-spread function photometric extraction using the `PIPE` package (see, e.g., A. Fortier et al. 2024).[17] We then performed a combined model using `cheoxplanet` (see, e.g., J. Egger et al. 2024).[18] In order to remove coherent variations caused by spacecraft rotation, an array of 24 independent flux parameters spaced evenly in roll angle (average spacing of 9°) is included in the model and a cubic spline drawn from these points is subtracted from the lightcurve.

Appendix B
Outlier Removal

Figure B1 shows the stellar spectrum from MIRI, time averaged over the fourth observation. The turnover below 5 μm is due to reduced throughput in slitless mode. The red "x" points indicate outliers in the spectrum that deviated from neighboring points in a nine-channel-wide sliding window by 3σ. These outliers were removed from the data as a first step before subsequent analysis.

Appendix C
Lightcurve Analysis

The target of these observations is an ephemeral cloud of dust and gas, rapidly evolving over the timescale of a single orbit ($\sim$9 hr), and the shape and depth of an individual transit deviates unpredictably from the classic solid-body transit model. Due to the unique nature of this object, subsequent analysis of the data was done using bespoke Python code to normalize and model the lightcurve transit. The time series output from `Eureka!` was curated by removing the first 30 minutes of data to account for instrument settling (T. Matsuo et al. 2019; T. J. Bell et al. 2023; J. Bouwman et al. 2023), and then removing $>3\sigma$ outliers from the stellar spectrum (see Figure B1).

Using the cleaned data, we first plotted the white lightcurve for each observation and identified a clear transit during the fourth expected transit window. Focusing first on the most significant detection, we modeled the transit in white light, and then applied this model to each channel in order to measure the spectroscopic depth. The primary model chosen is a simple second-degree polynomial over the transit window that goes to zero at the window edges. The average lightcurve from the original K2 data, a skewed Gaussian, and a simple boxcar were also tested as models, resulting in no significant difference in the derived spectrum, verifying that our results are not sensitive to this choice.

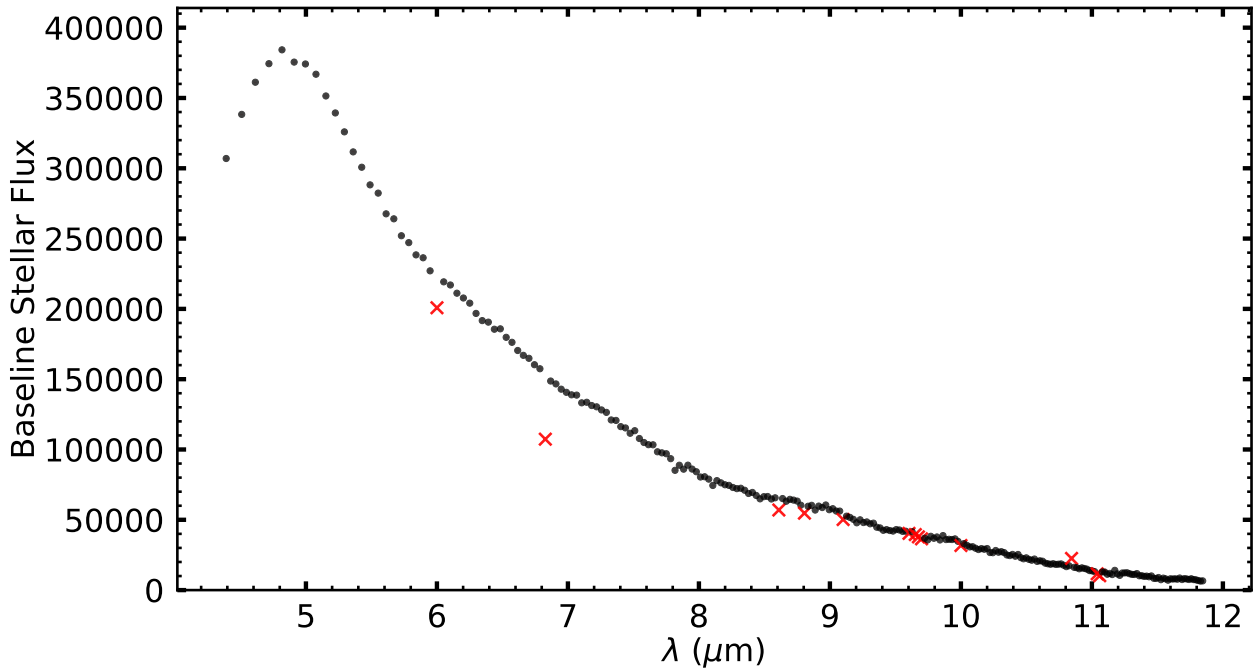


Figure B1. Time-averaged stellar spectrum with flux outliers removed. The turnover below 5 μm is due to reduced throughput. A sliding window of nine channels was used to identify points with a greater than 3σ deviation from its neighbors. Red "x" points are the outliers that were removed.

[17] https://github.com/alphapsa/PIPE
[18] https://github.com/hposborn/chexoplanet

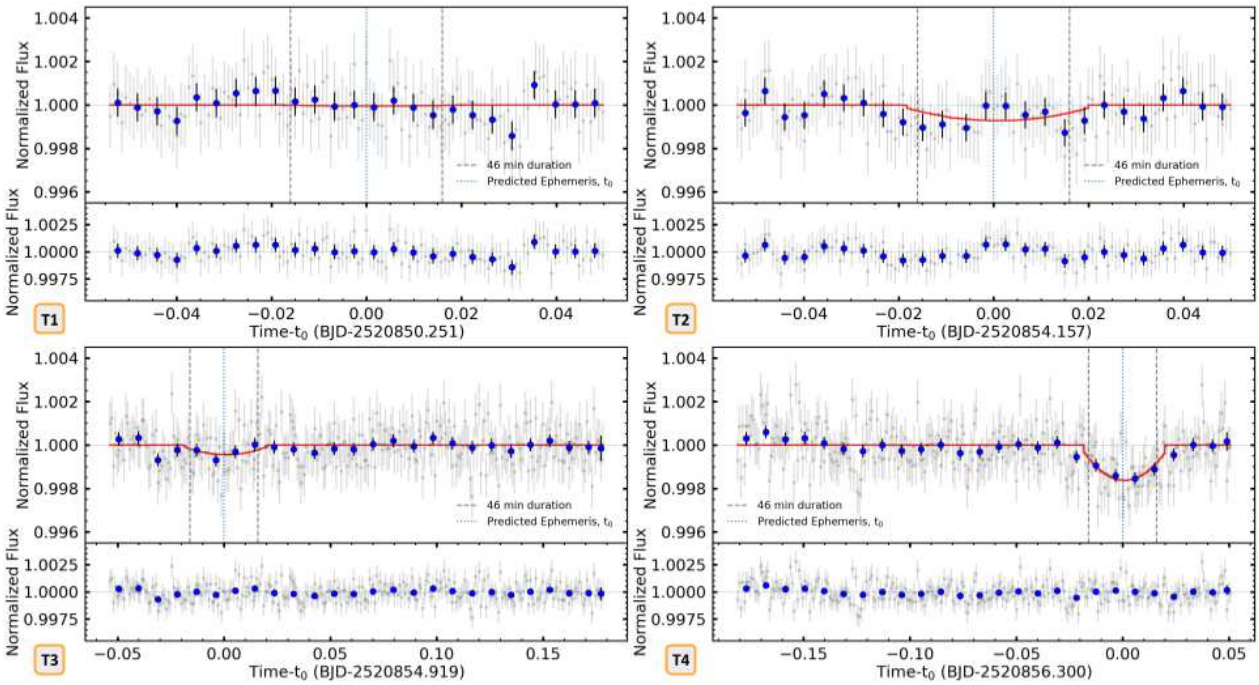


Figure C1. MIRI LRS lightcurves for all four transit observations listed in Tables 1 and 2 for combined light of the spectral channels up to 8 μm. The unbinned data (at a cadence of 72 s) are grayed out in the background. The blue points are binned to a time resolution of 8 minutes. The red line is a second-order polynomial fit to transit 4 and scaled to the best-fit value in each window. Multiple transit models were fit, including the original K2 lightcurve, a skewed Gaussian, and a boxcar, with no significant difference in the overall depth or resulting spectrum. The 46 minute transit duration calculated by R. Sanchis-Ojeda et al. (2015) is included as vertical gray dashed lines for reference. The uncertainties in the data points as reported by `Eureka!` were inflated to match the actual standard deviation in the baseline flux.

The model depth, δ, was calculated from

$$\delta = \frac{\sum_i (y_i - 1) f_i / \sigma_i^2}{\sum_i f_i^2 / \sigma_i^2}, \tag{C1}$$

where y is the measured normalized flux, f is the model, and σ is the uncertainty in each data point, as measured by the standard deviation of the baseline flux. Due to the unknown extent of the transiting cloud, the baseline flux was conservatively chosen outside 1.5× the 46 minute transit duration window calculated by R. Sanchis-Ojeda et al. (2015) and centered at the ephemeris from E. Schlawin et al. (2021). The model depth variance, σ_δ^2, is calculated as

$$\sigma_\delta^2 = \frac{1}{\sum_i f_i^2 / \sigma_i^2}. \tag{C2}$$

We then applied these same techniques to the lightcurves and spectra of the other observations.

Figure C1 shows the cleaned time series data for all four transit observations described in Section 2 and listed in Table 2, for the combined light of the MIRI spectral channels up to 8 μm. The first 30 minutes of data were removed from each observation to account for settling. The baseline of each observation was conservatively estimated as the flux outside 1.5× the 46 minute average transit duration determined by R. Sanchis-Ojeda et al. (2015). For observations 1, 2, and 3, a line was fit to the baseline flux and divided out to detrend any residual ramp remaining after the `Eureka!` pipeline reduction. The reported uncertainties from `Eureka!` were inflated to match the standard deviation in the baseline flux. By increasing the reported uncertainties, as opposed to simply using the standard deviation in the data, we hoped to preserve any variations due to systematics that were properly accounted for in the reduction pipeline. We applied this same treatment of each time series in both the combined-light and the individual spectral channels for each observation.

Multiple bin sizes were tried, and we ultimately settled on binning to a time resolution of 8 minutes ($N = 21$). Figure C2 shows the results of plotting the standard deviation of the residuals of the model fit versus bin size, illustrating the absence of significant red noise. We constructed a lightcurve model by fitting a second-degree polynomial to these binned up points in the transit window of transit 4, and setting the model to the mean of the baseline flux elsewhere. This model was then applied to each transit observation, centered around the ephemeris and scaled to measure the transit depth. These measurements are listed in Table 2. The residuals for these models are shown in the bottom panels of each lightcurve in Figure C1. Other lightcurve models were also tested, including the average K2 lightcurve, a skewed Gaussian, and a simple boxcar. The resulting spectra from fitting these models to the spectroscopic channels showed no significant difference, indicating our results are not sensitive to our choice of lightcurve model.

The "look elsewhere" plots in Figure C3 show the results of taking the transit model, fixed in duration and allowing the depth to vary, and sliding it across the time series of the combined light of the MIRI spectral channels up to 8 μm for each observation to measure the depth at every point. Equations (C1) and (C2) are used to calculate the depth and uncertainty at each point, respectively. With tighter uncertainties and larger deviations from the normalized flux, the most significant depth measurement occurs during the fourth predicted transit window. These results also lend additional

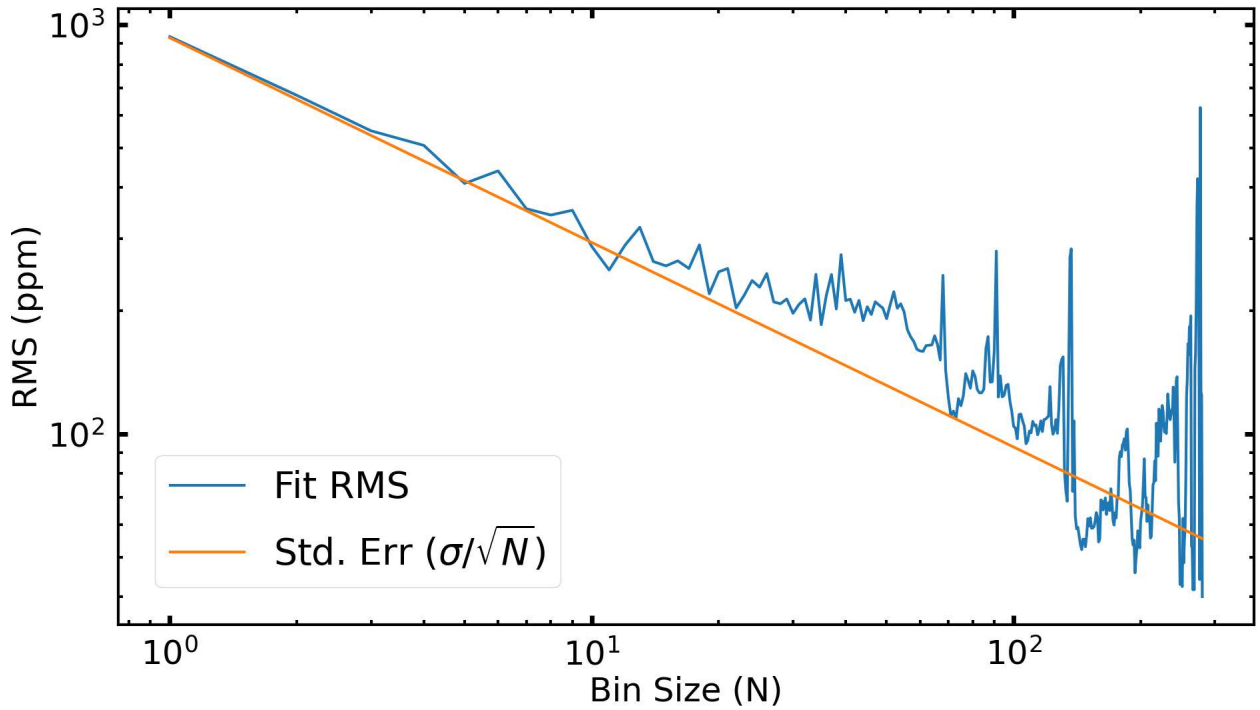


Figure C2. A standard assessment of the residuals of the model fit to the lightcurve for transit 4 using the combined light of the MIRI spectral channels up to 8 μm. The blue line shows the rms of the residuals of the transit model fit to the data for different bin sizes. The unbinned data were taken with a cadence of 72 s, providing roughly 38 points across the assumed average transit duration. The orange line shows how our adopted single measurement uncertainty would scale as white noise as the data are binned up. The uncertainties in the data points as reported by `Eureka!` were inflated by a factor to match the actual standard deviation in the baseline flux for more conservatively accurate error estimates while preserving variations in the measurements.

support for the low-significance detections during the second and third transit windows. To account for differences between the isolated observations and the full phase curve, which are evident in the different noise profiles, we treated the distributions separately to examine the red noise. The standard deviation in the measured depths elsewhere is $\lesssim$1.1$\times$ the uncertainty in our reported measurements listed in Table 2, consistent with the absence of red noise shown in Figure C2. We therefore ignore the contribution of red noise in our analysis as a negligible effect. These results support our report of a transit detection during the fourth transit window.

The same lightcurve models were tested on the CHEOPS photometry, also showing no significant difference in the results. However, three of the four transits of K2-22 b were impacted by Earth occultation gaps in our observing windows. Only the fourth transit window, and fortuitously the most significant transit event, lined up with an unobstructed observing window for CHEOPS. Figure C4 shows the fit of our chosen second-degree polynomial model to the detrended CHEOPS data over the transit window. We measured the depth and associated uncertainty of each transit fit using Equations (C1) and (C2). The magnitude of K2-22 b ($G = 14.93$) is technically beyond the rated ($G = 6-12$) magnitude limit of CHEOPS (A. Fortier et al. 2024). The result was a photometric lightcurve with an rms of 2371 ppm per 30 minute bin. Given the CHEOPS bandpass of 330–1100 nm, we added this photometric point to our JWST spectrum as an optical depth constraint.

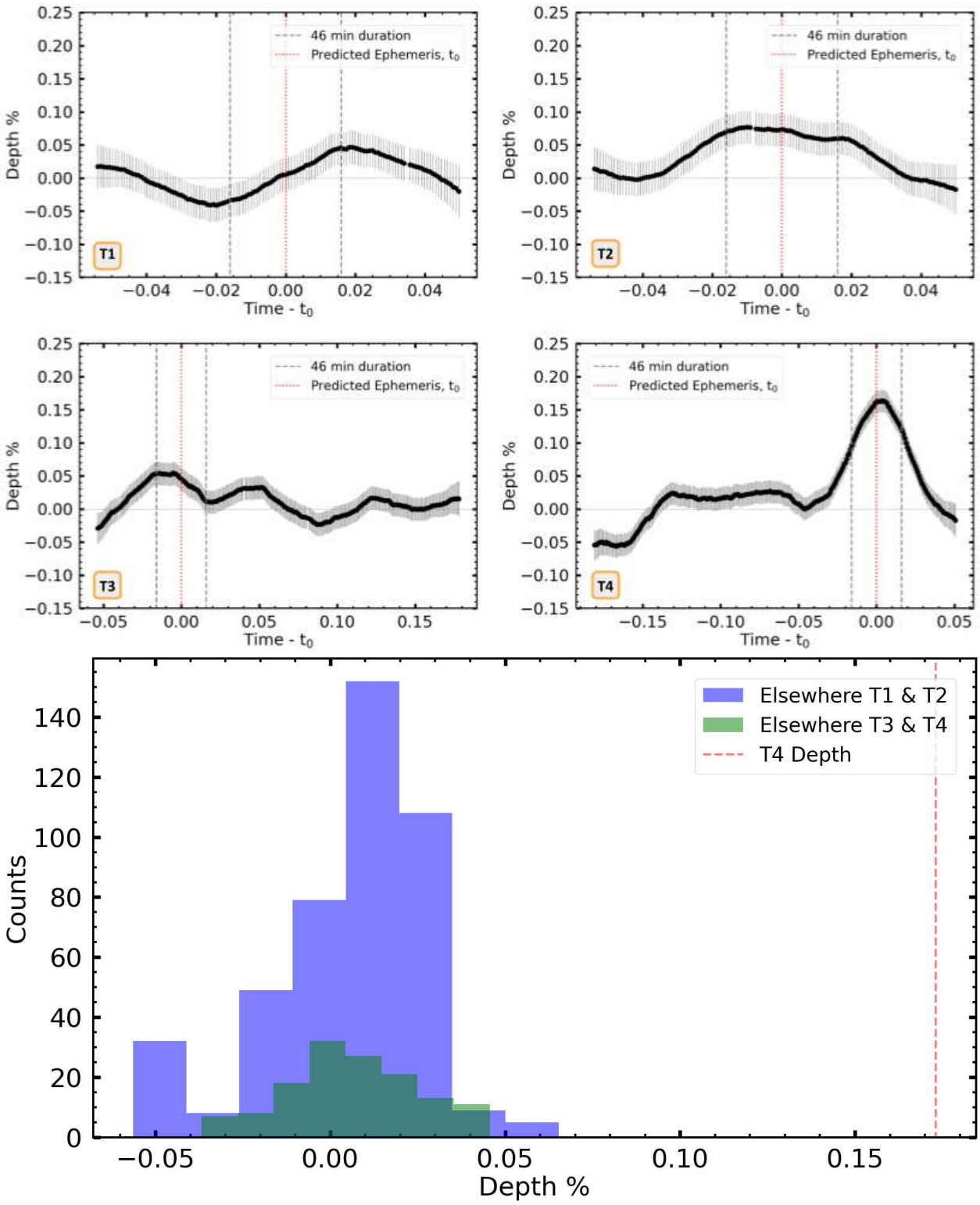


Figure C3. Top: measured depth using the transit model as a fixed-duration sliding window across the combined-light time series for each observation up to 8 μm. This shows that there is some variation in the normalized flux for each transit, possibly due to systematics from MIRI. The most significant measurement occurs at the predicted transit center time of the fourth transit window, while low-significance measurements in transit windows 2 and 3 correspond to those reported in Section 3. Bottom: histogram of depth measurements (blue) at all times outside 1.5× the 46 minute duration of each transit window, i.e., "elsewhere" in the observations. The stand-alone observations, 1 and 2, show distinctly increased uncertainties and are thus treated separately from the full phase curve. The standard deviations in the distributions are $\lesssim$1.1× the calculated depth uncertainty, suggesting minimal effects from red noise. The red dashed line shows the measured depth at the center time of the fourth transit window for comparison.

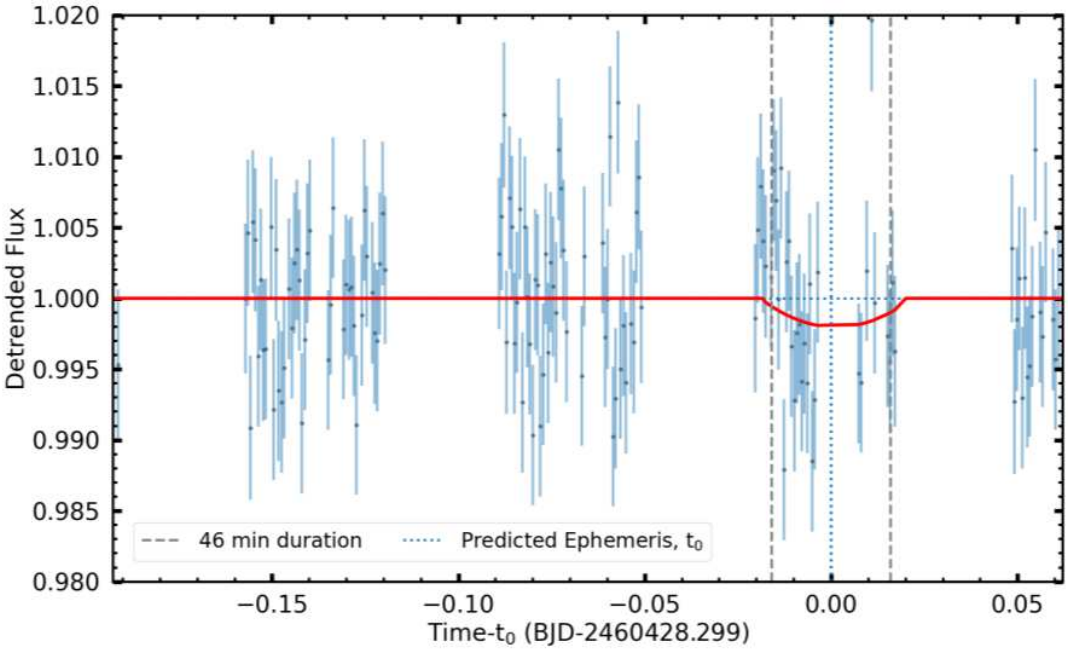


Figure C4. Detrended CHEOPS photometry during transit 4. The red line is a second-order polynomial fit to the transit window and zero elsewhere. Multiple transit models were fit, including the original K2 lightcurve, a skewed Gaussian, and a boxcar, with no significant difference. The 46 minute transit duration calculated by R. Sanchis-Ojeda et al. (2015) is included for reference. Gaps in the data were caused by occultations of Earth during the space telescope's orbit. The other three transit windows fall in these gaps.

Appendix D
Supporting Evidence for Spectral Features

The resulting spectrum appears consistent with some combination of solid mineralogy over the wavelength range of 4.4–8 μm with additional gas opacity to explain the short-wavelength features (4.4–5.3 μm), see Sections 3.1 and 3.2. Due to the large uncertainties at the longer wavelengths, it is difficult to differentiate between the different solid mineralogies. However, Figure D1 shows the results of the calculations of the BIC for a select group of mineralogy using

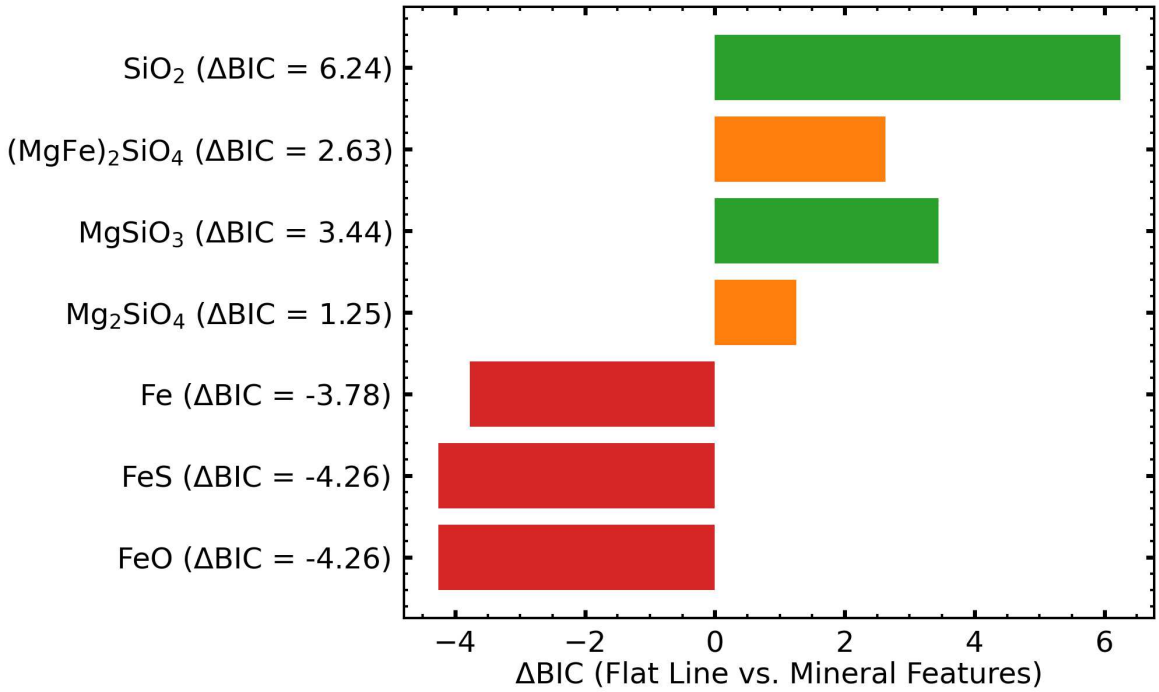


Figure D1. Calculated ΔBIC values for select solid mineralogy opacities noted in Section 3.1 and shown in Figure 3 against a flat line as compared with our resulting spectrum at wavelengths < 8 μm. The top four models shown here, quartz (SiO_2 [s]), olivine ($(MgFe)_2SiO_4$ [s]), enstatite ($MgSiO_3$ [s]), and forsterite (Mg_2SiO_4 [s]), represent likely crust/mantle minerals. The bottom three, iron (Fe [s]), iron sulfide (FeS [s]), and iron oxide (FeO [s]), represent likely core minerals. We used two parameters to scale and offset the mineralogy models, and one parameter for the flat line. These ΔBIC values show that the spectrum data are more consistent with mantle mineralogy than either a flat spectrum or iron-dominant mineralogy. The different colored bars are a qualitative comparison of the results; negative values are shown in red, positive values below three are colored orange, and those above three are green.

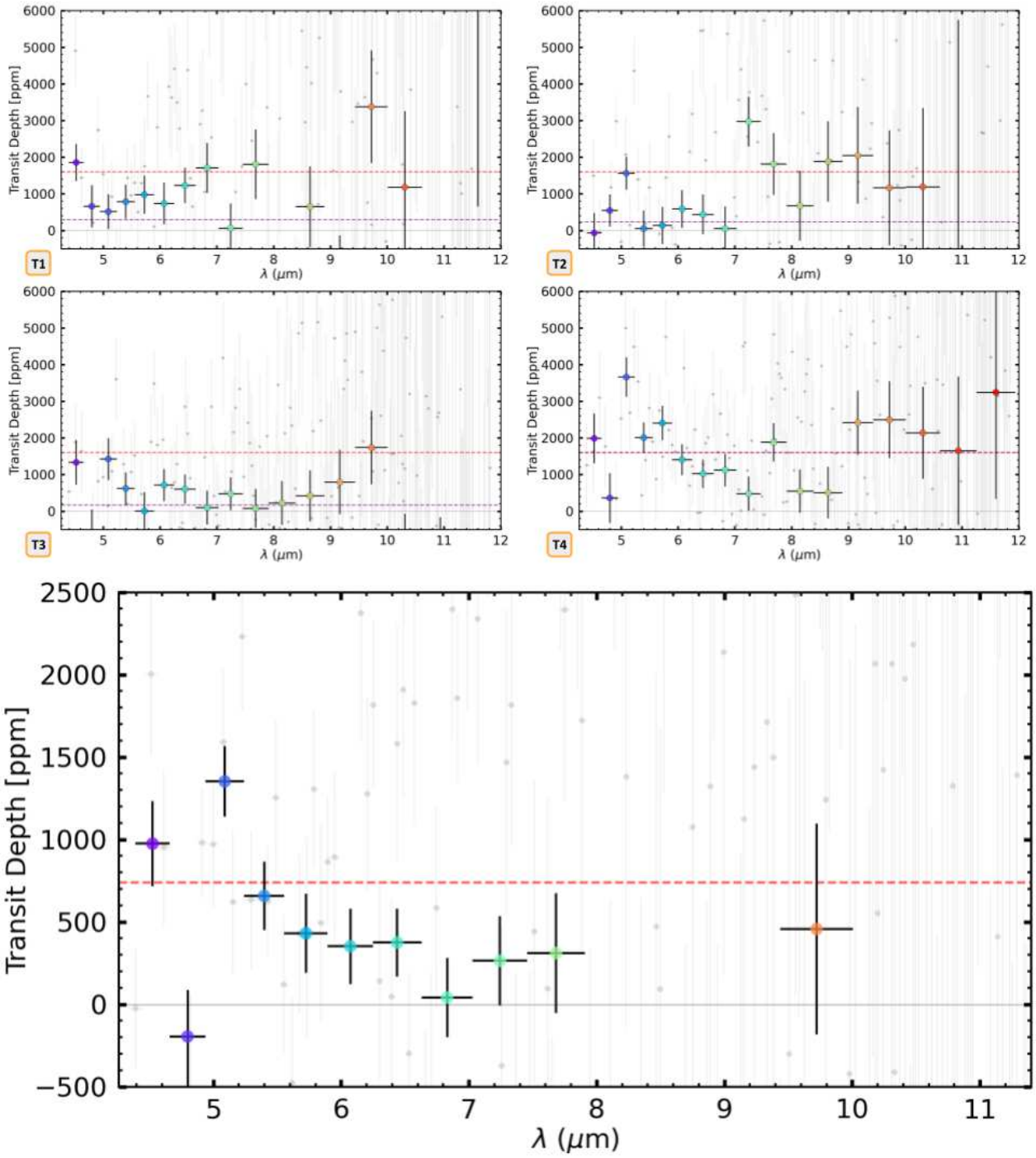


Figure D2. MIRI spectra during all four expected transits using the second-degree transit model from transit 4, scaled to the optimal depth in each channel for each transit. Top: individual spectra during each transit window. The red dashed line marks the overall transit depth in transit 4. The purple dashed line indicates the overall transit depth in each observation as measured from the white-light lightcurves. The white-light time series of transit 4 shows a clear signal, while the others do not (see Figure C1). However, the most or second most significant detections in transit 1, transit 2, and transit 3 are in the 4.5 and 5.1 μm channels, supporting the reality of these narrow features observed at modest significance in transit 4. Bottom: combined spectra of all four transits. The 4.5 and 5.1 μm features are clearly evident.

two parameters to scale and offset the models as compared with a flat line with just one parameter. There is a positive significance for some mantle-like silicate mineralogy over an iron-dominated core-like mineralogy or flat spectrum. We performed the same test over the entire 4.4–11.8 μm range, which favors the magnesium-rich silicates, while still disfavoring the iron-dominated core-like species. From this we conclude that our spectrum is more consistent with mantle mineralogy features than a featureless flat spectrum.

The short-wavelength channels are prone to some amount of contamination due to spectral foldover from the LRS disperser element, a double prism assembly (P. Bouchet et al. 2022). The lowest bin in our JWST $R = 17$ spectrum at 4.52 μm contains spectral channels 4.39, 4.51, and 4.61 μm. Figure 10

from P. Bouchet et al. (2022) shows that below 4.5 μm there is significant contamination from the flux in channels blueward of the foldover point at 3.9 μm. We estimate that the lowest bin in our JWST spectrum, containing the three shortest wavelength channels, could be contaminated by up to ~30% from flux between 3.25 and 3.5 μm. Our next shortest bin, indicating significant transparency and including channels 4.72, 4.82, and 4.91 μm, could be contaminated by up to ~11% from flux between 3.0 and 3.25 μm. The most interesting and significant feature at 5.1 μm includes channels 5.00, 5.08, and 5.15 μm, and could be contaminated by up to ~6% from wavelengths less than 3 μm. A more precise evaluation of the strength of the features that correspond to our data would necessitate a more rigorous analysis of the potential contamination from spectral foldover and subsequent increased uncertainties. However, spectral foldover is unlikely to significantly affect our value of the opacity in the 4.52 μm bin, since the signal at 3.25–3.5 μm is being diluted by a factor of at least 3. This further motivates the necessity to validate these short-wavelength features with follow-up measurements, particularly with overlapping wavelength coverage in the near-infrared.

Our assessment of the short-wavelength features is discussed in Section 3.2, and here we offer additional support for our results. The white-light time series for observation 1 shows no transit, and observations 2 and 3 show only low-significance ($<3\sigma$) transits in combined light over the reduced wavelength range of 4.4–8 μm. Despite little to no evidence for white-light transit detections in these observations, we produced a spectrum for each transit window by fitting our transit model to each spectral channel. The top panel of Figure D2 shows the resulting fit for each observation. The data are binned the same for each observation ($R = 17$) and show significant depth in the 4.5 and 5.1 μm channels in transits 1, 2, and 3, despite their low overall white-light transit depth. And in every observation, the spectra show transparency in the 4.8 μm bin.

The bottom panel of Figure D2 shows a stacked spectrum of all four transits. To stack these spectra we first added the time series flux in each channel centered around the ephemeris for each observation. We then fit our transit model to the combined time series flux in each channel and binned as before ($R = 17$) to produce the combined spectrum. The most significant features are still present at 4.5 and 5.1 μm even with reduced overall white-light transit depth.

We applied the same "look elsewhere" technique described in Appendix C and shown in Figure C3 to test the depth measurements in each spectral channel. Similar to the results in combined light, we find that the standard deviation in measured depths is 1.5× the uncertainty we are reporting. The significance of the feature in the 5.1 μm bin as shown in the JWST spectrum in Figure 2 is 6.8σ, or 4.5σ with a 1.5× increase in the uncertainties.

Appendix E
Optical Data References

Table E1 lists the references for the optical data used to derive opacities for each mineralogical species.

Table E1
Dust Optical Data Sources

Condensate	References
Al_2O_3 [s]	B. Begemann et al. (1997)[a,b]; C. Koike et al. (1995)[b]
$CaTiO_3$ [s]	T. Posch et al. (2003)[b]; K. Ueda et al. (1998)[c]
Fe [s]	Lynch & Hunter in E. D. Palik (1991)[b]
$Fe_{0.4}Mg_{0.6}O$ [s]	T. Henning et al. (1995)[a,b]
$Fe_{0.7}Mg_{0.3}O$ [s]	T. Henning et al. (1995)[a,b]
Fe_2SiO_4 [s]	unpublished[a]
FeO [s]	T. Henning et al. (1995)[a,b]
FeS [s]	J. B. Pollack et al. (1994)[b]; T. Henning & H. Mutschke (1997)[b]
Mg_2SiO_4 [s]	C. Jäger et al. (2003)[a,b]
$MgSiO_3$ [s]	C. Jäger et al. (2003)[a,b]
$MgAl_2O_4$ [s]	S. Zeidler et al. (2011); Tropf & Thomas in E. D. Palik (1991)[b]
SiC [s]	A. Laor & B. T. Draine (1993)[b]
SiO_2 [s]	T. Henning & H. Mutschke (1997)[a,b]; section Philipp in E. D. Palik (1985)[b]

Notes. For details on the wavelength ranges please refer to Table 1 in D. Kitzmann & K. Heng (2018). We note we use the amorphous (sol-gel) data for Mg_2SiO_4[s] and $MgSiO_3$[s], and the amorphous data for SiO_2[s].
[a] Data from the Database of Optical Constants for Cosmic Dust, Laboratory Astrophysics Group of the Astrophysical Institute and University Observatory, orAIU) Jena.
[b] Data from a printed or digital table.
[c] Data from a figure.

ORCID iDs

Nick Tusay https://orcid.org/0000-0001-9686-5890
Jason T. Wright https://orcid.org/0000-0001-6160-5888
Thomas G. Beatty https://orcid.org/0000-0002-9539-4203
Steve Desch https://orcid.org/0000-0002-1571-0836
Knicole Colón https://orcid.org/0000-0001-8020-7121
Tushar Mittal https://orcid.org/0000-0002-8026-0018
Hugh P. Osborn https://orcid.org/0000-0002-4047-4724
Beatriz Campos Estrada https://orcid.org/0000-0003-0225-1201
James E. Owen https://orcid.org/0000-0002-4856-7837
Jessica Libby-Roberts https://orcid.org/0000-0002-2990-7613
Arvind F. Gupta https://orcid.org/0000-0002-5463-9980
Brad Foley https://orcid.org/0000-0002-6943-3192
Erik Meier Valdés https://orcid.org/0000-0002-2160-8782
Daniel J. Stevens https://orcid.org/0000-0002-5951-8328
Ashley Herbst https://orcid.org/0000-0002-6051-9002

References

Adibekyan, V., Dorn, C., Sousa, S. G., et al. 2021, Sci, 374, 330
Astropy Collaboration, Price-Whelan, A. M., Lim, P. L., et al. 2022, ApJ, 935, 167
Astropy Collaboration, Price-Whelan, A. M., Sipőcz, B. M., et al. 2018, AJ, 156, 123
Astropy Collaboration, Robitaille, T. P., Tollerud, E. J., et al. 2013, A&A, 558, A33
Ballmer, M. D., & Noack, L. 2021, Eleme, 17, 245
Beatty, T. G., Welbanks, L., Schlawin, E., et al. 2024, ApJL, 970, L10
Begemann, B., Dorschner, J., Henning, T., et al. 1997, ApJ, 476, 199
Bell, T. J., Ahrer, E.-M., Brande, J., et al. 2022, JOSS, 7, 4503
Bell, T. J., Kreidberg, L., Kendrew, S., et al. 2023, arXiv:2301.06350

Benz, W., Broeg, C., Fortier, A., et al. 2021, ExA, 51, 109
Bodman, E. H., Wright, J. T., Desch, S. J., & Lisse, C. M. 2018, AJ, 156, 173
Booth, R. A., Owen, J. E., & Schulik, M. 2023, MNRAS, 518, 1761
Bouchet, P., Gastaud, R., & Lagage, P. O. 2022, Proc. SPIE, 12180, 121800Z
Bouwman, J., Kendrew, S., Greene, T. P., et al. 2023, PASP, 135, 038002
Bromley, J., & Chiang, E. 2023, MNRAS, 521, 5746
Bulak, M., Paardekooper, D., Fedoseev, G., et al. 2022, A&A, 657, A120
Campos Estrada, B., Owen, J. E., Jankovic, M. R., Wilson, A., & Helling, C. 2024, MNRAS, 528, 1249
Carnahan, E., Vance, S. D., Hesse, M. A., Journaux, B., & Sotin, C. 2022, GeoRL, 49, e97602
Chazallon, B., & Pirim, C. 2018, ChEnJ, 342, 171
Cockell, C. S., Simons, M., Castillo-Rogez, J., et al. 2024, NatAs, 8, 675
Colón, K. D., Zhou, G., Shporer, A., et al. 2018, AJ, 156, 227
Curry, A., Booth, R., Owen, J. E., & Mohanty, S. 2024, MNRAS, 528, 4314
Curry, A., Mohanty, S., & Owen, J. E. 2025, MNRAS, 536, 913
De Sanctis, M. C., Ammannito, E., Carrozzo, F., et al. 2024, ComEE, 5, 131
Diab, J., Daswani, M. M., & Castillo-Rogez, J. 2023, Icar, 391, 115339
Dorn, C., Khan, A., Heng, K., et al. 2015, A&A, 577, A83
Egger, J., Osborn, H., Kubyshkina, D., et al. 2024, A&A, 688, A223
Foley, B. J. 2024, RvMG, 90, 559
Fortier, A., Simon, A., Broeg, C., et al. 2024, A&A, 687, A302
Gaidos, E., Parviainen, H., Esparza-Borges, E., et al. 2024, A&A, 688, L34
Grimm, S. L., Malik, M., Kitzmann, D., et al. 2021, ApJS, 253, 30
Henning, T., Begemann, B., Mutschke, H., & Dorschner, J. 1995, A&AS, 112, 143
Henning, T., & Mutschke, H. 1997, A&A, 327, 743
Hon, M., Rappaport, S., Shporer, A., et al. 2025, ApJ, 984, 3
Hughes, A. M., Duchêne, G., & Matthews, B. C. 2018, ARA&A, 56, 541
Jäger, C., Dorschner, J., Mutschke, H., Posch, T., & Henning, T. 2003, A&A, 408, 193
Johnson, B., & Goldblatt, C. 2015, ESRv, 148, 150
Journaux, B., Kalousová, K., Sotin, C., et al. 2020, SSRv, 216, 7
Jura, M., & Young, E. D. 2014, AREPS, 42, 45
Kargel, J. S., & Lewis, J. S. 1993, Icar, 105, 1
Kawahara, H., Hirano, T., Kurosaki, K., Ito, Y., & Ikoma, M. 2013, ApJL, 776, L6
Keil, K. 1965, Natur, 207, 745
Kite, E. S., Fegley, B., Jr., Schaefer, L., & Gaidos, E. 2016, ApJ, 828, 80
Kitzmann, D., & Heng, K. 2018, MNRAS, 475, 94
Koike, C., Kaito, C., Yamamoto, T., et al. 1995, Icar, 114, 203
Kulterer, B. M., Wampfler, S. F., Ligterink, N. F. W., et al. 2024, A&A, 691, A281
Laor, A., & Draine, B. T. 1993, ApJ, 402, 441
Lee, M. R., Russell, S. S., Arden, J. W., & Pillinger, C. T. 1995, Metic, 30, 387
Marsh, D., Solomon, S., & Reynolds, A. 2004, JGRA, 109, A7
Matsuo, T., Greene, T. P., Johnson, R. R., et al. 2019, PASP, 131, 124502
McDonough, W. F., & Sun, S.-s. 1995, ChGeo, 120, 223
Meerdink, S. K., Hook, S. J., Roberts, D. A., & Abbott, E. A. 2019, RSEnv, 230, 111196
Mendis, D. A., & Horányi, M. 2013, RvGeo, 51, 53
Mie, G. 1908, AnP, 330, 377
Miguel, Y., Kaltenegger, L., Fegley, B., & Schaefer, L. 2011, ApJL, 742, L19
Mysen, B. 2019, PEPS, 6, 1
Nathues, A., Hoffmann, M., Sarkar, R., et al. 2024, JGRE, 129, e2023JE008150
O'Neill, H. S. C., & Palme, H. 1998, Composition of the Silicate Earth: Implications for Accretion and Core Formation (Cambridge: Cambridge Univ. Press), 3
Palik, E. D. 1985, Handbook of Optical Constants of Solids (New York: Academic Press),
Palik, E. D. 1991, Handbook of Optical Constants of Solids II (New York: Academic Press),
Perez-Becker, D. A. 2013, PhD thesis, Univ. of California, Berkeley
Pollack, J. B., Hollenbach, D., Beckwith, S., et al. 1994, ApJ, 421, 615
Posch, T., Kerschbaum, F., Fabian, D., et al. 2003, ApJS, 149, 437
Rappaport, S., Barclay, T., DeVore, J., et al. 2014, ApJ, 784, 40
Rappaport, S., Levine, A., Chiang, E., et al. 2012, ApJ, 752, 1
Rothman, L. S., Gordon, I. E., Barbe, A., et al. 2009, JQSRT, 110, 533
Sanchis-Ojeda, R., Rappaport, S., Pallè, E., et al. 2015, ApJ, 812, 112
Scarpa, R., Tilling, R. I., & Giggenbach, W. 1996, Monitoring and Mitigation of Volcano Hazards (Berlin: Springer), 675
Schaefer, L., & Fegley, B. 2009, ApJL, 703, L113
Schlawin, E., Herter, T., Zhao, M., Teske, J. K., & Chen, H. 2016, ApJ, 826, 156
Schlawin, E., Hirano, T., Kawahara, H., et al. 2018, AJ, 156, 281
Schlawin, E., Mukherjee, S., Ohno, K., et al. 2024a, AJ, 168, 104
Schlawin, E., Ohno, K., Bell, T. J., et al. 2024b, ApJL, 974, L33
Schlawin, E., Su, K. Y. L., Herter, T., Ridden-Harper, A., & Apai, D. 2021, AJ, 162, 57
Seager, S., Kuchner, M., Hier-Majumder, C. A., & Militzer, B. 2007, ApJ, 669, 1279
Sinnhuber, M., Nieder, H., & Wieters, N. 2012, SGeo, 33, 1281
Swain, M. R., Hasegawa, Y., Thorngren, D. P., & Roudier, G. M. 2024, SSRv, 220, 61
Thiabaud, A., Marboeuf, U., Alibert, Y., Leya, I., & Mezger, K. 2015, A&A, 580, A30
Ueda, K., Yanagi, H., Noshiro, R., Hosono, H., & Kawazoe, H. 1998, JPCM, 10, 3669
van Lieshout, R., Min, M., & Dominik, C. 2014, A&A, 572, A76
van Lieshout, R., Min, M., Dominik, C., et al. 2016, A&A, 596, A32
Vanderburg, A., Johnson, J. A., Rappaport, S., et al. 2015, Natur, 526, 546
Wang, H. S., Liu, F., Ireland, T. R., et al. 2019, MNRAS, 482, 2222
Welbanks, L., Bell, T. J., Beatty, T. G., et al. 2024, Natur, 630, 836
Wu, S. C., Dewberry, J. W., & Fuller, J. 2024, ApJ, 963, 34
Zeidler, S., Posch, T., Mutschke, H., Richter, H., & Wehrhan, O. 2011, A&A, 526, A68